ADVANCES IN ATMOSPHERIC SCIENCES, VOL. 32, JULY 2015, 991–1004

# Cloud-Base Distribution and Cirrus Properties Based on Micropulse Lidar Measurements at a Site in Southeastern China

Jianjun LIU[1,2,3], Zhanqing LI[*1,2], ZHENG Youfei[3], and Maureen CRIBB[2]

[1]*State Laboratory of Earth Surface Process and Resource Ecology and College of Global Change and Earth System Science, Beijing Normal University, Beijing* 100875

[2]*Earth System Science Interdisciplinary Center, University of Maryland, College Park, Maryland,* 20740*, USA*

[3]*Jiangsu Key Laboratory of Atmospheric Environment Monitoring and Pollution Control, Nanjing University of Information Science and Technology, Nanjing* 210044

(Received 09 August 2014; revised 11 November 2014; accepted 5 December 2014)

ABSTRACT

The cloud fraction (CF) and cloud-base heights (CBHs), and cirrus properties, over a site in southeastern China from June 2008 to May 2009, are examined by a ground-based lidar. Results show that clouds occupied the sky 41% of the time. Significant seasonal variations in CF were found with a maximum/minimum during winter/summer and similar magnitudes of CF in spring and autumn. A distinct diurnal cycle in the overall mean CF was seen. Total, daytime, and nighttime annual mean CBHs were $3.05 \pm 2.73$ km, $2.46 \pm 2.08$ km, and $3.51 \pm 3.07$ km, respectively. The lowest/highest CBH occurred around noon/midnight. Cirrus clouds were present ∼36.2% of the time at night with the percentage increased in summer and decreased in spring. Annual mean values for cirrus geometrical properties were $8.89 \pm 1.65$ km, $9.80 \pm 1.70$ km, $10.73 \pm 1.86$ km and $1.83 \pm 0.91$ km for the base, mid-cloud, top height, and the thickness, respectively. Seasonal variations in cirrus geometrical properties show a maximum/minimum in summer/winter for all cirrus geometrical parameters. The mean cirrus lidar ratio for all cirrus cases in our study was $\sim 25 \pm 17$ sr, with a smooth seasonal trend. The cirrus optical depth ranged from 0.001 to 2.475, with a mean of $0.34 \pm 0.33$. Sub-visual, thin, and dense cirrus were observed in ∼12%, 43%, and 45% of the cases, respectively. More frequent, thicker cirrus clouds occurred in summer than in any other season. The properties of cirrus cloud over the site are compared with other lidar-based retrievals of midlatitude cirrus cloud properties.

**Key words**: cloud-base distribution, cirrus properties, lidar, southeastern China

**Citation**: Liu, J. J., Z. Q. Li, Y. F. Zheng, and M. Cribb, 2015: Cloud-base distribution and cirrus properties based on micropulse lidar measurements at a site in southeastern China. *Adv. Atmos. Sci.*, **32**(7), 991–1004, doi: 10.1007/s00376-014-4176-2.

## 1. Introduction

The significant influences of clouds on the redistribution of energy and moisture, atmospheric dynamics, thermodynamics, and the hydrological cycle on regional and global scales by means of scattering and absorbing radiation and releasing latent heat mainly depend on their spatio–temporal variations in vertical structure and horizontal distribution (Stephens, 2005; Dong et al., 2005). Among the multiple cloud types, cirrus clouds play an important role in Earth's climate and cover 17%–30% of Earth's atmosphere (Dessler and Yang, 2003; Sassen et al., 2008). The frequency of occurrence of cirrus clouds can reach 45% in the tropics (Stubenrauch et al., 2006). Cirrus clouds in the upper troposphere have two opposite effects: an infrared greenhouse effect and a solar albedo effect, which strongly depend on their macrophysical and optical properties. The radiative and climate effects of clouds, especially cirrus clouds, still remain largely uncertain. A clear understanding of their macrophysical and optical properties at different geographical locations is essential for climate modeling studies (Giannakaki et al., 2007). Satellite-based passive remote sensing, such as that performed by the Moderate Resolution Imaging Spectroradiometer (MODIS), has enabled the observation of cloud characteristics such as the amount and top height on a global scale (Platnick et al., 2003). However, their retrieval accuracy suffers from various limitations (Chang and Li, 2005). Passive satellite sensors with visible and near-infrared channels have difficulty inferring the properties of low and optically thin clouds (Wu et al., 2009). Spaceborne active remote sensors, such as CloudSat and Cloud-Aerosol Lidar Pathfinder Satellite Observations (CALIPSO), can provide information about cloud vertical structure worldwide (Winker et al., 2003; Mace et al., 2009), but the temporal resolution is limited, making any investigation of the diurnal cycle of clouds over specific regions impossible (Min et al., 2010).

Ground-based instruments can capture the diurnal cycle

* Corresponding author: Zhanqing LI
Email: 11112010133@bnu.edu.cn

of clouds and are valuable for monitoring long-term trends at fixed locations. Although ground-based lidars cannot penetrate optically thick clouds or determine cloud-top heights, they can detect the presence of clouds and measure lowest layer cloud-base heights (CBH). Numerous studies have demonstrated their ability to observe cloud properties (Campbell and Shiobara, 2008; Shupe et al., 2011; Thorsen et al., 2013), and in particular, to quantify and characterize the vertical structure and optical properties of cirrus clouds. Lidar observations provide information on cloud vertical structure with a much higher sensitivity to optically thin clouds than a cloud radar (Thorsen et al., 2013). The capability of a ground-based lidar system to detect thin cirrus clouds makes it one of the most appropriate instruments to use for the study of these clouds (Noel et al., 2007).

Using ground-based lidar data, many studies have been carried out regarding the temporal and spatial variations of cloud structure (Mahesh et al., 2005; Bissonnette et al., 2007; Shupe et al., 2011) and macro- and microphysical and optical properties, as well as radiative effects of cirrus clouds over different regions, such as the tropics (Sassen and Campbell, 2001; Comstock et al., 2002; Seifert et al., 2007; Sunilkumar et al., 2008) and the midlatitudes (Reichardt, 1999; Keckhut et al., 2005; Wang et al., 2008; Das et al., 2009; Dupont et al., 2010). Significant differences in cloud characteristics exist from one region to another and the representation of clouds in climate models is still poor (Zhang et al., 2005). Characterizing the spatial and temporal distributions of clouds with better spatial and temporal resolutions, including the macrophysics and optical properties of cirrus clouds at different geographic locations, is fundamental to understanding and quantifying the roles of clouds in climate change and in improving weather climate models (IPCC, 2007; Vukicevic et al., 2010).

During the deployment of the United States Department of Energy's Atmospheric Radiation Measurement Mobile Facility in China (Li et al., 2011), extensive measurements were made at Taihu from May 2008 to December 2009 for the purpose of studying aerosol–cloud interactions under heavily polluted conditions. The site (31.702°N, 120.358°E; 10 m above sea level) is located in the heart of the Yangtze Delta, where there is an abundance of different types of anthropogenic aerosols (Li et al., 2007). To help unravel aerosol–cloud interactions, cloud and aerosol properties were measured by numerous advanced instruments installed at the site. By virtue of continuous ground-based lidar measurements, we investigate the cloud-base distribution and geometrical and optical properties of cirrus clouds with the goal of laying the foundations for studying aerosol–cloud interactions.

The remainder of the paper is organized as follows. Section 2 describes the micropulse lidar system and methods used to determine the cloud mask and to retrieve cirrus optical properties. Seasonal patterns and the diurnal cycle of the cloud-base distribution are discussed in section 3. Section 4 presents the seasonal evolution of the vertical structure, macrophysical properties, and optical properties of cirrus clouds. Section 5 gives the main conclusions.

## 2. Instruments and methods

A depolarization-sensitive micropulse lidar (MPL), which is a compact and solid state lidar developed at NASA and manufactured by the Sigma Space Corporation, was used (Spinhirne et al., 1995). It uses an Nd: YLF pulsed laser diode, operating at a wavelength of 527 nm with a pulse repetition rate of 2500 Hz. The bin time of the MPL receiver was 200 ns, with a 30 m vertical resolution. The MPL system averages many low-energy pulses in short durations to achieve a good signal-to-noise ratio (SNR). A pulsed solid-state laser, a narrow field-of-view (FOV: ~100 μrad), narrow interference filters (~0.3 nm full width at half maximum), and photon counting capability result in a highly sensitive instrument. Further detail regarding the features of the MPL can be found in Spinhirne et al. (1995).

Figure 1 shows the steps taken to retrieve cloud properties in this study. Using the method described by Campbell et al. (2002), raw data were corrected to the normalized relative backscatter signal (NRB). Lidar signals at upper-tropospheric ranges are significantly influenced by the afterpulse. To minimize this influence, afterpulse calibrations were performed frequently using the methods proposed by Campbell et al. (2002) and Liu et al. (2011). Cloud boundaries were derived using the cloud mask algorithm of Wang and Sassen (2001). This algorithm is based on characteristics of the lidar signal, as in the differential zero-crossing and threshold methods, and also takes into account the underlying physical differences between cloud and aerosol layers, and noise effects. To distinguish a cloud layer from an aerosol layer, empirical threshold values were used (Clothiaux et al., 1998; Campbell et al., 2002; Zhao et al., 2014). Use of these values in the algorithm proved successful at separating clouds from aerosols with high accuracy. More detail is given in Wang and Sassen (2001). Cirrus optical properties were retrieved using the algorithm of Comstock and Sassen (2001), which is based on the solution of the lidar equation. The cloud backscatter coefficient, $\beta_c$ (km sr$^{-1}$), is given by

$$\beta_c(z) = \frac{G(z_0,z)}{1-2\eta k\int_{z_0}^{z} G(z_0,z)dz} - \beta_m(z)\ ,$$

$$G(z_0,z) = \beta_m(z_0)\frac{S(z)z^2}{S(z_0)z_0^2}\times\exp\left[2\left(\frac{8\pi}{3}-\eta k\right)\int_{z_0}^{z}\beta_m(z)dz\right],$$

where $\beta_m$ is the scattering contribution from air molecules, $S(z)$ is the normalized lidar backscatter signal, and $\eta$ and $k$ are the forward multiple-scattering correction parameter and the extinction-to-backscatter ratio, respectively. $z_0$ denotes the height just below the cloud base where the scattering is presumably due to molecules, and $z$ is the height at which the backscatter signals are received. The parameter $k$ is determined using an iterative technique where the value of $k$ is increased incrementally from 5 to 100 sr. It reaches its final value when the average backscatter coefficient above the cloud is equal to the average molecular backscatter coefficient above the cloud.

The optical depth of the cirrus cloud, $\tau_c$, can be determined by integrating $\beta_c$ between the cirrus cloud base, $z_b$,

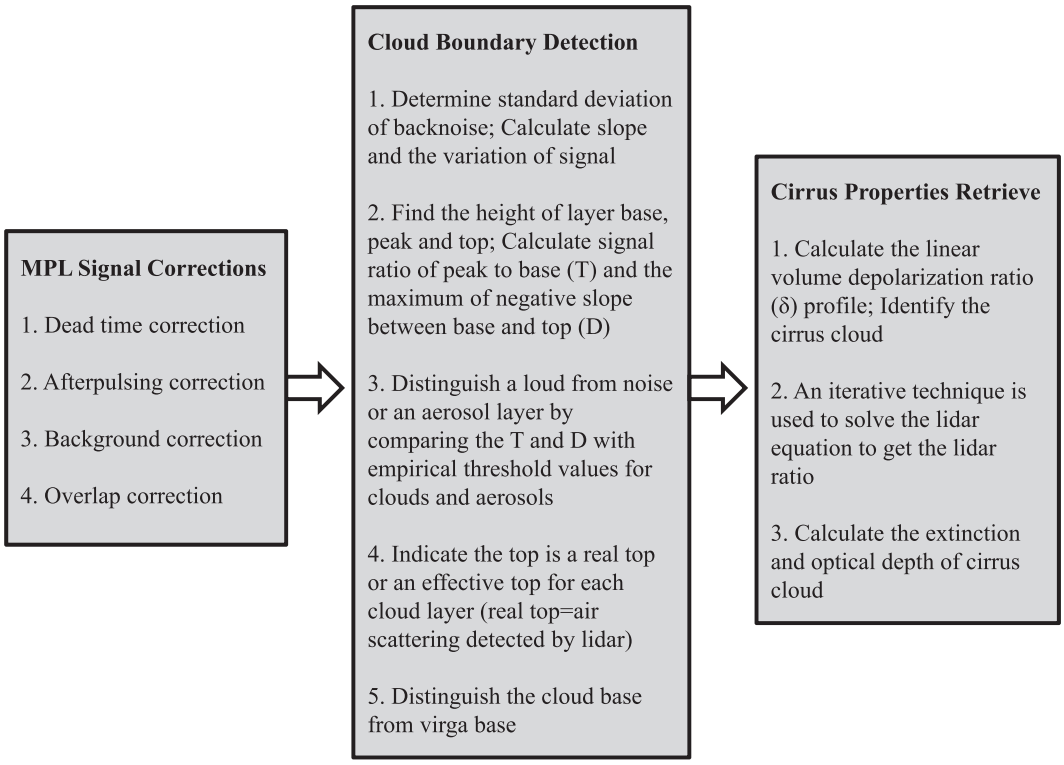


**Fig. 1.** Diagram of the steps taken to retrieve cloud properties in this study.

and the cloud top, $z_t$. The primary uncertainty in the $\tau_c$ retrieval is in estimating the parameter $k$, which results in a maximum uncertainty of ∼24% for the retrieved value of $\tau_c$ (Comstock and Sassen, 2001). This algorithm has been applied to several long-term datasets in both the midlatitudes and the tropics with reasonable accuracy (Sassen and Comstock, 2001; Comstock et al., 2002). The forward multiple-scattering correction parameter was used to compensate for the effect of forward multiple-scattering on the return energy. The contribution of forward multiple-scattering to the total cloud optical depth was assumed to be relatively small here because the MPL receiving telescope has a narrow FOV (Das et al., 2009). In this study, we set $\eta = 0.9$ based on simulations of the multiple scattering correction factor by Comstock and Sassen (2001).

The linear volume depolarization ratio ($\delta$), defined as the ratio of cross-polarized and co-polarized scattering ratios, was computed from MPL measurements using the method of Flynn et al. (2007). This quantity is useful for studying the shape of ice crystals and provides dynamical information about cloud formation.

## 3. Cloud fraction and cloud-base distribution

### 3.1. *Cloud fraction*

The cloud fraction (CF) is defined here as the percentage of returns that are identified as cloudy within a specified sampling period (e.g., a month) regardless of the number of cloud layers. Although lidar-derived CF represents only a pencil beam of the sky that depends on the advection of clouds overhead, studies have found that they are statistically representative in terms of long-term averages (Dong et al., 2006, 2010).

Figure 2a shows the monthly mean CF from June 2008 to May 2009 with seasonal and annual mean values summarized in Table 1. CF varied significantly throughout the year. CF peaked during February, October and March, with values larger than 50% and reached a minimum during June and July, with values around 25%. The largest CF (∼67.2%) was more than 2.5 times greater than the smallest CF (25.4%). The annual averaged CF was 40.6% and the seasonal mean CF was marked by maxima during winter and minima during summer (Table 1). The CF seasonal variability reflects the difference in large-scale atmospheric dynamics between the summer and the winter and transition periods (Kollias et al., 2007). A similar CF and the same seasonal variation in CF were also found at another midlatitude site, the Southern Great Plains (SGP) site in the U. S. (Dong et al., 2006). Monthly (Fig. 2b) and seasonal (Table 1) mean daytime and nighttime CF show that more clouds occurred during the night than during the day. On average, the largest seasonal CF for daytime and nighttime occurred in winter and spring, and the smallest values for both were found in summer. Annual mean daytime and nighttime CFs were 17.9% and 22.7%, respectively, during the entire study period.

Seasonal and annual mean diurnal cycles of the CF anomaly, defined as the difference between hourly and daily mean CF, are presented in Fig. 3. The annual average CF anomaly experienced a significant diurnal cycle with ampli-

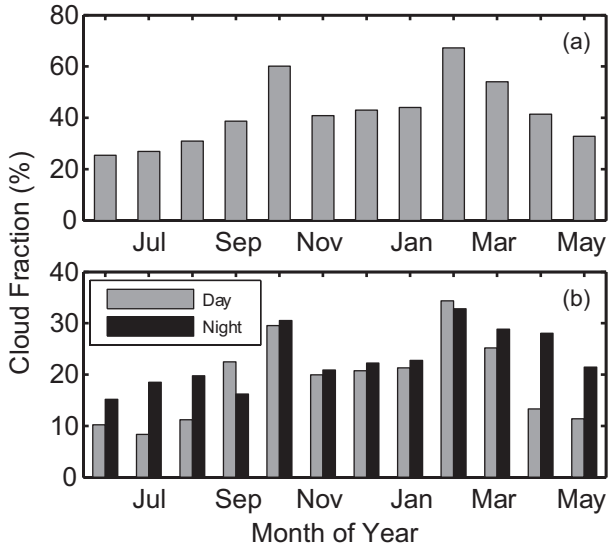


**Fig. 2.** Monthly variation in (a) mean cloud fraction (b) during the day (0600–1800 LST) and during the night (1800–0600 LST) over Taihu from June 2008 to May 2009.

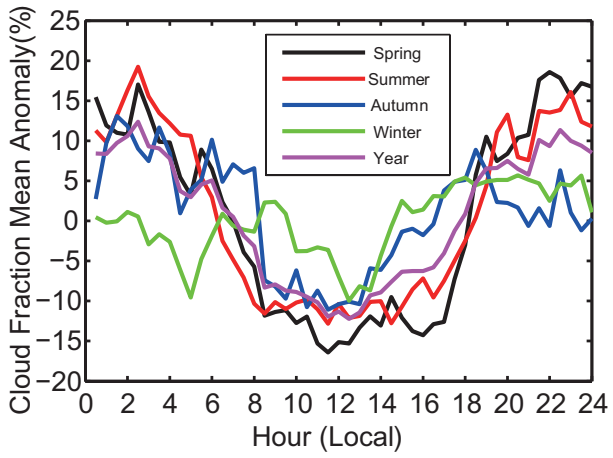


**Fig. 3.** Seasonal and annual mean diurnal cycles of the cloud fraction mean anomaly (hourly mean minus daily mean) over Taihu from June 2008 to May 2009.

tudes of about 24.6%. The annual average CF anomaly decreased sharply from the beginning of the day to midday, and then gradually increased again. Maxima in the CF anomaly occurred at around 0200 and 2200 LST and the minimum occurred at around local noon. This is possibly related to an increase in solar heating at the cloud top at noon resulting in a relative stabilization of the cloud layer leading to somewhat less cloudiness (Shupe et al., 2011). Concerning the seasonal diurnal cycle, a strong diurnal variation can be seen in spring, summer, and autumn with amplitudes of 35.0%, 32.1%, and 24.2%, respectively. A relatively moderate diurnal variation was found in winter with amplitude of about 15.7%, which is partly due to the weak local convection at the surface in wintertime (Dong et al., 2005). Generally speaking, seasonal patterns in the variation of the diurnal CF mean anomaly are similar to the annual pattern, except for wintertime. In winter, the minimum CF mean anomaly occurred at 0500 LST and around 1200 LST, with a sharp variation between the beginning of the day and the late afternoon, followed by a leveling off for the remainder of the night. Although similar variations are found in spring, summer and autumn, differences in the relative variation are seen. For example, in summer, the variation was smoother before and after noon than it was during spring and autumn.

### 3.2. *Cloud-base distribution*

Due to the severe attenuation in lidar signals by thick clouds, the analysis of cloud bases presented here refers to the analysis of the first cloud layer base detected from the ground regardless of the number of cloud layers above it. Monthly statistics of total (T), daytime (D), and nighttime (N) CBH, with annual means given on the right-hand side of the plot (shaded), are summarized in Fig. 4. Seasonal and annual means, standard deviations, and median values of CBH for T, D, and N cases are shown in Table 1. Relatively high annual mean CBHs were found, with mean values of $3.05 \pm 2.73$ (T), $2.46 \pm 2.08$ (D), and $3.51 \pm 3.07$ km (N). The highest annual mean CBH was found during the night. Monthly variations in the mean CBH for all cases were almost the same, with the

**Table 1.** Seasonal and annual mean cloud fraction (CF) and cloud-base height (CBH) in three altitude bins (L, M, H)* based on total (T), daytime (D), and nighttime (N) observations. Also included are the seasonal and annual mean probability distribution functions (PDFs) in the three altitude bins.

| | CF (T) | CF (D) | CF (N) | CBH (T)** (Median) | CBH (D)** (Median) | CBH (N)** (Median) | PDF (L) | PDF (M) | PDF (H) |
|---|---|---|---|---|---|---|---|---|---|
| Spring | 42.7% | 16.6% | 26.1% | $3.74 \pm 2.75$ 3.09 | $2.86 \pm 2.05$ 2.25 | $4.30 \pm 2.98$ 3.63 | 35.8% | 34.3% | 29.9% |
| Summer | 27.7% | 9.9% | 17.8% | $3.98 \pm 3.57$ 2.77 | $2.74 \pm 2.63$ 1.57 | $4.68 \pm 3.82$ 3.52 | 41.5% | 25.8% | 32.7% |
| Autumn | 46.5% | 24.0% | 22.5% | $2.35 \pm 2.03$ 1.59 | $2.20 \pm 1.82$ 1.50 | $2.51 \pm 2.22$ 1.71 | 57.7% | 31.3% | 11.0% |
| Winter | 51.4% | 25.5% | 25.9% | $2.23 \pm 2.11$ 1.35 | $2.22 \pm 1.96$ 1.45 | $2.24 \pm 2.24$ 1.29 | 60.8% | 27.6% | 11.6% |
| Year | 40.6% | 17.9% | 22.7% | $3.05 \pm 2.73$ 2.07 | $2.46 \pm 2.08$ 1.74 | $3.51 \pm 3.07$ 2.40 | 48.9% | 30.3% | 20.8% |

*L, M, H: cloud-base heights located below 2 km, between 2 km and 5 km, and above 5 km, respectively.

**Mean values of cloud-base height. Units: km.

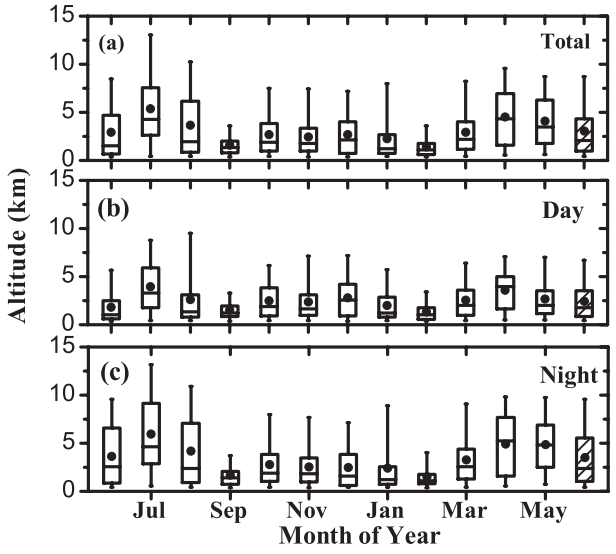


**Fig. 4.** Monthly and annual (ANN) mean cloud-base heights for (a) all clouds, (b) daytime clouds, and (c) nighttime clouds over Taihu from June 2008 to May 2009. Box and whisker plots include the median (middle of the box), 25th and 75th percentiles (ends of the box), 5th and 95th percentiles (ends of the whiskers), and the mean (black dots).

highest values in the spring and summer, and especially during the nighttime period (Table 1). Because monthly/seasonal distributions of CBH are strongly skewed towards higher values, monthly/seasonal median values are typically lower, although the same general trends are seen (Shupe et al., 2011). Similar seasonal patterns in CBH, i.e., maximum/minimum values in summer/winter, have been found at other sites, e.g., the SGP site (Dong et al., 2005), the South Pole (Mahesh et al., 2005), and Eureka in the Arctic (Shupe et al., 2011).

Probability distribution functions (PDFs) of monthly and annual mean CBH, given in 0.5 km vertical range bins, are shown in Fig. 5. Seasonal and annual mean PDFs for three different altitude ranges (below 2 km, 2–5 km, and above 5 km) are listed in Table 1. Looking at the annual mean vertical distribution, the largest number of detected cloud bases (∼17%) falls within the surface-based temperature inversion (0.5–1 km). A similar result was reported by Dong et al. (2005) at the SGP site. Annual mean vertical probability distributions gradually decrease with increasing height above 1 km. Annual mean PDFs of CBH within the three height ranges were about 48.9%, 30.3%, and 20.8%, respectively (Table 1).

The monthly and annual diurnal cycles of mean CBH are plotted in Fig. 6. CBHs were averaged over a half-hour period in this study. The diurnal cycle of CBH in summer and spring varied greatly throughout the day. CBHs hit a minimum around noon and reached a maximum around midnight. The strongest signatures were seen in July. The highest CBH occurred from 0030 to 0100 LST and the lowest CBH occurred between 1100 and 1130 LST. The difference between the highest and lowest CBH was 5.1 km. The daily range in CBH during autumn and winter was not as dramatic. For example, in February, changes in CBH throughout the day were less than 1.1 km. The diurnal cycle in CBH was weak in autumn and in winter. The annual diurnal cycle in mean CBH (Fig. 6b) has the same features as the variation in CBH during spring and summer. From 0300 to 1000 LST, a marked decrease in CBH occurred, and from 1700 to 2100 LST a sharp increase was seen.

## 4. Cirrus cloud properties

To differentiate between water clouds and cirrus clouds, the following three criteria are used to identify cirrus clouds: (1) CBH is greater than 7 km; (2) $\delta$ is greater than 0.03 (Das et al., 2010); and (3) the maximum $\tau_c$ is less than 3.0 (Sassen and Campbell, 2001). Only nighttime data are used here because, during the day, the signal-to-noise ratio is poor at high altitudes due to contamination by background pho-

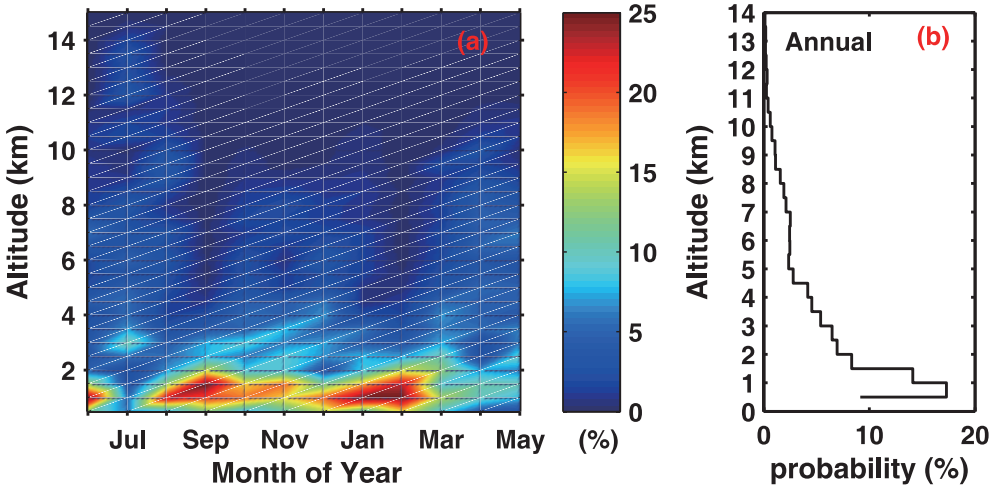


**Fig. 5.** Probability distribution functions of (a) monthly and (b) annual mean cloud-base heights over Taihu from June 2008 to May 2009. Cloud-base heights were averaged over 0.5 km bins in the vertical direction.

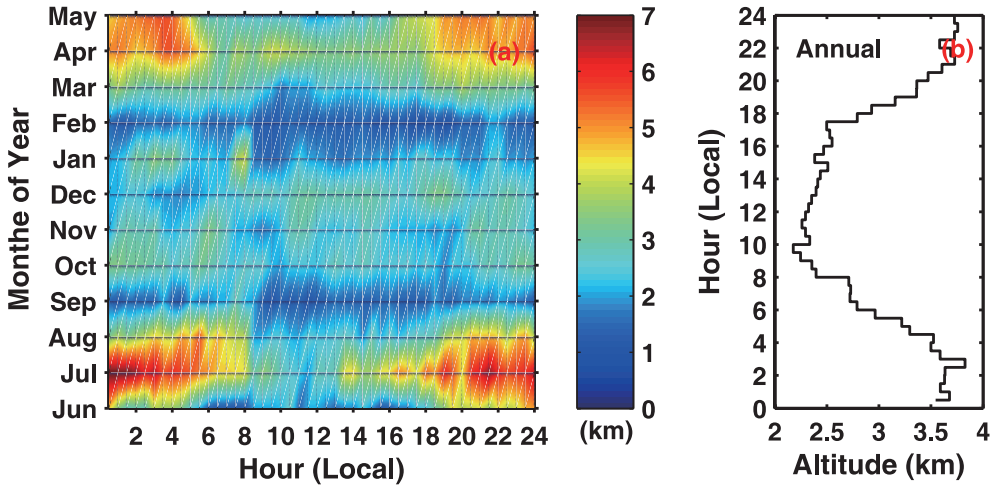


**Fig. 6.** (a) Monthly and (b) annual mean diurnal cycles of mean cloud-base heights over Taihu from June 2008 to May 2009. Cloud-base heights were averaged over 30 minutes.

ton counts (Dupont et al., 2011). The cirrus occurrence fraction is defined as the ratio of the number of nights that cirrus was detected to the total number of nights measurements were made. Cirrus clouds were identified in 42, 45, 17, and 13 nights out of a total of 83, 87, 85, and 68 nights during spring, summer, autumn, and winter, respectively. This corresponds to cirrus occurrence fractions of 50.6%, 51.7%, 20%, and 19.1%, respectively. The annual mean cirrus occurrence fraction was 36.2%. A maximum cirrus occurrence in summer and a minimum in winter were also found from two years' worth of Cloud-Aerosol Lidar with Orthogonal Polarization (CALIOP) data over northern China (Min et al., 2011). The summertime maximum happens because there is a relatively abundant supply of upper-tropospheric water vapor introduced by regional convective activity influenced by the western tropical Pacific and because of the seasonal meridional displacement of subtropical cirrus bands (Sassen et al., 2008; Min et al., 2011). The annual mean cirrus occurrence in our study is similar to that (37%) calculated from an eight-year cirrus climatology generated by Das et al. (2009) over Chung-Li, a site in East Asia.

### 4.1. *Cirrus geometrical properties*

Figure 7 shows the following cirrus geometrical properties in the form of box plots: (a) CBH, (b) mid-cloud height; (c)cloud-top height, and (d) geometrical thickness in each month and year-round. Seasonal and annual mean cirrus geometrical properties and vertical probability distributions of cirrus geometrical properties are summarized in Table 2 and plotted in Fig. 8. The mid-cloud height is the weighted CBH, which is defined as

$$M = \frac{\int_{z_{\rm base}}^{z_{\rm top}} z R_{\rm B}(z) dz}{\int_{z_{\rm base}}^{z_{\rm top}} R_{\rm B}(z) dz} .$$

Here, $z_{\rm base}$ and $z_{\rm top}$ correspond to CBH and CTH, respectively, and $z$ is the height at which the backscatter signals are received. The parameter $R_{\rm B}(z)$ is the backscattering ratio, which can be expressed as

$$R_{\rm B}(z) = \frac{\beta_{\rm c}(z) + \beta_{\gamma}(z)}{\beta_{\gamma}(z)} ,$$

where $\beta_{\gamma}(z)$ and $\beta_{\rm c}(z)$ are the backscattering coefficients of air and cloud at the laser wavelength, respectively.

Figures 7a and 7b show that cirrus base and mid-cloud heights varied greatly by month. Maximum and minimum monthly mean cirrus base (mid-cloud) heights of $10.8 \pm 2.2$ km ($11.8 \pm 2.2$ km) and $7.7 \pm 0.6$ km ($8.4 \pm 0.6$ km) occurred in July and December, respectively. For most of the year, cloud-base and mid-cloud height distributions were strongly skewed towards higher values because median values were typically lower, although the same general trends are seen (Shupe et al., 2011). Seasonal mean cirrus cloud-base heights (mid-cloud heights) were $8.38 \pm 1.02$ km ($9.21 \pm 0.99$ km), $9.89 \pm 1.97$ km ($10.97 \pm 1.93$ km), $7.94 \pm 0.71$ km ($8.66 \pm 0.69$ km), and $7.75 \pm 0.60$ km ($8.40 \pm 0.61$ km) in spring, summer, autumn, and winter, respectively, with an annual mean of $8.89 \pm 1.65$ km ($9.80 \pm 1.70$ km) during the course of the study (Table 2). The vertical distribution of summertime cloud-base heights shows a broad distribution in summer ranging from 7 km to 14.3 km and a relatively smooth variation with height. For other seasons, about 62.7% (spring), 82.8% (autumn) and 89.4% (winter) of cirrus cloud bases are located below 8.5 km. Figure 8b shows that the vertical occurrence of mid-cloud heights also experienced a smooth variation with height in summer, with peaks at 8.5 km and 12.5–13 km. In spring, around 81.5% of mid-cloud heights fell between 8.0 and 10.5 km, and about 87.5% and 93.0% of mid-cloud heights varied between 7.5 km and 9.5 km in autumn and winter. From data over the whole year, cirrus base and mid-cloud heights ranged from 7 km to 14.3 km and from 7.1 km to 15 km, respectively. The majority of cirrus base heights ($\sim$56%) and mid-cloud heights ($\sim$50%) were located in the range of 7–8.5 km and 8–9.5 km, respectively.

Cirrus cloud-top heights (CTHs) also experienced significant monthly variations (Fig. 7c). Mean CTHs were $10.08 \pm$

**Table 2.** Seasonal and annual averages, standard deviations, and median values of cirrus base height (BH), top height (TH), mid-height (MH), and geometrical thickness (GT).

| | BH (km) | | MH (km) | | TH (km) | | GT (km) | |
|---|---|---|---|---|---|---|---|---|
| | Mean ± std | Median | Mean ± std | Median | Mean ± std | Median | Mean ± std | Median |
| Spring | 8.38 ± 1.02 | 8.09 | 9.21 ± 0.99 | 8.92 | 10.08 ± 1.07 | 9.95 | 1.69 ± 0.76 | 1.65 |
| Summer | 9.89 ± 1.97 | 9.44 | 10.97 ± 1.93 | 10.90 | 12.10 ± 1.98 | 12.22 | 2.22 ± 0.97 | 2.17 |
| Autumn | 7.94 ± 0.71 | 7.76 | 8.66 ± 0.69 | 8.59 | 9.25 ± 0.80 | 9.26 | 1.31 ± 0.72 | 1.26 |
| Winter | 7.75 ± 0.60 | 7.64 | 8.40 ± 0.61 | 8.37 | 8.99 ± 0.75 | 8.81 | 1.24 ± 0.57 | 1.26 |
| Year | 8.89 ± 1.65 | 8.33 | 9.80 ± 1.70 | 9.24 | 10.73 ± 1.86 | 10.22 | 1.83 ± 0.91 | 1.77 |

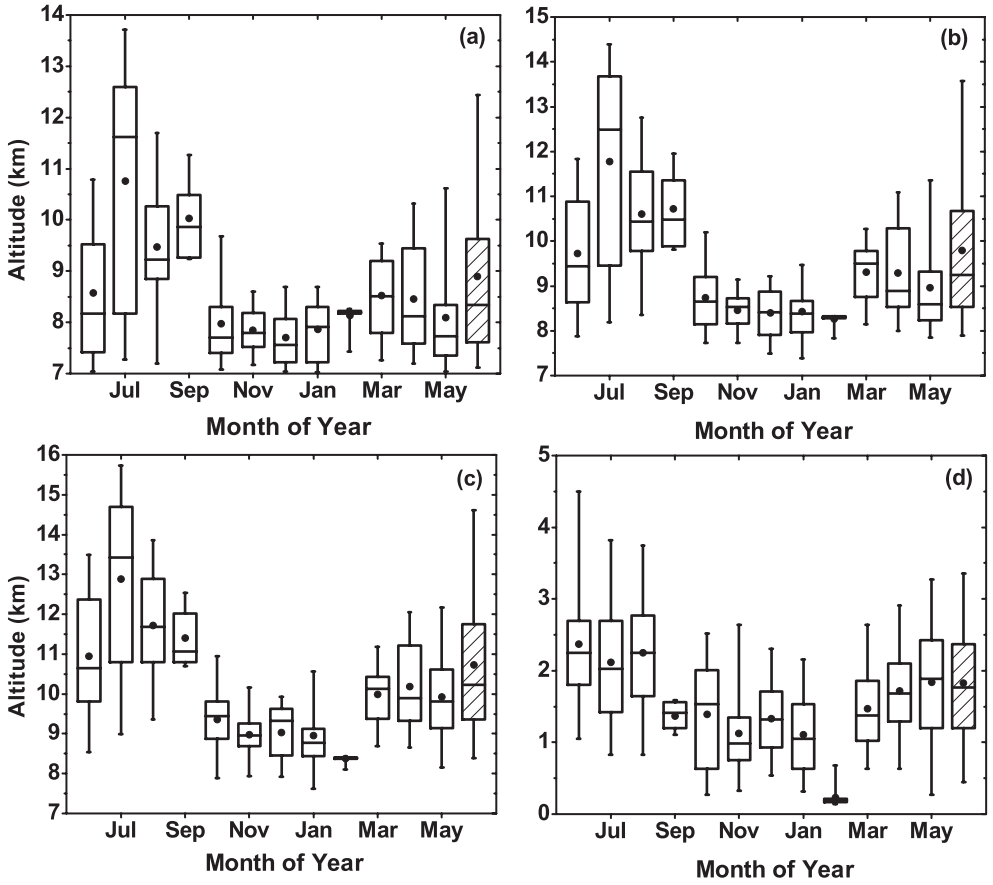


**Fig. 7.** The same as Fig. 4, but for cirrus geometrical properties: (a) cloud-base height; (b) mid-cloud height; (c) cloud-top height; (d) geometrical thickness.

1.07 (spring), 12.10 ± 1.98 (summer), 9.25 ± 0.80 (autumn) and 8.99 ± 0.75 km (winter), with an annual mean of 10.73 ± 1.86 km. Figure 8c shows that CTHs had a broad (7–16 km) and multimodal distribution, with a major mode centered on the 13–13.5 km height range in summer. Nearly 70% and more than 90% of CTHs in spring and in autumn and winter, respectively, were located below 10.5 km. Most CTHs (more than 40%) reached an altitude of 9–10.5 km during the study period.

Cirrus geometrical thickness monthly and annual statistics are shown in Fig. 7d. There is a noticeable month-to-month variation. Maximum (minimum) values are found in summer (autumn). The annual mean thickness was 1.83 ± 0.91 km and seasonal mean thicknesses were 1.69 ± 0.76 (spring), 2.22 ± 0.97 (summer), 1.31 ± 0.72 (autumn), and 1.24 ± 0.57 km (winter). The PDF for cirrus thickness in each season (Fig. 8d) has a distribution with one mode and thicknesses are mostly less than 5 km (spring), 6 km (summer), 3.5 km (autumn) and 3 km (winter). Peaks in thickness were found in 26.1% of the cases in spring (1.5–2 km), 23.8% of the cases in summer (2–2.5 km), 22.0% of the cases in autumn (1–1.5 km), and 35.1% of the cases in winter (1–1.5 km). In terms of the annual PDF, approximately 86.2% of the cases studied had thicknesses between 0.5 km and 3 km.

### 4.2. *Cirrus optical properties*

Cirrus optical properties, including the extinction-to-backscattering ratio (commonly known as the lidar ratio, LR),

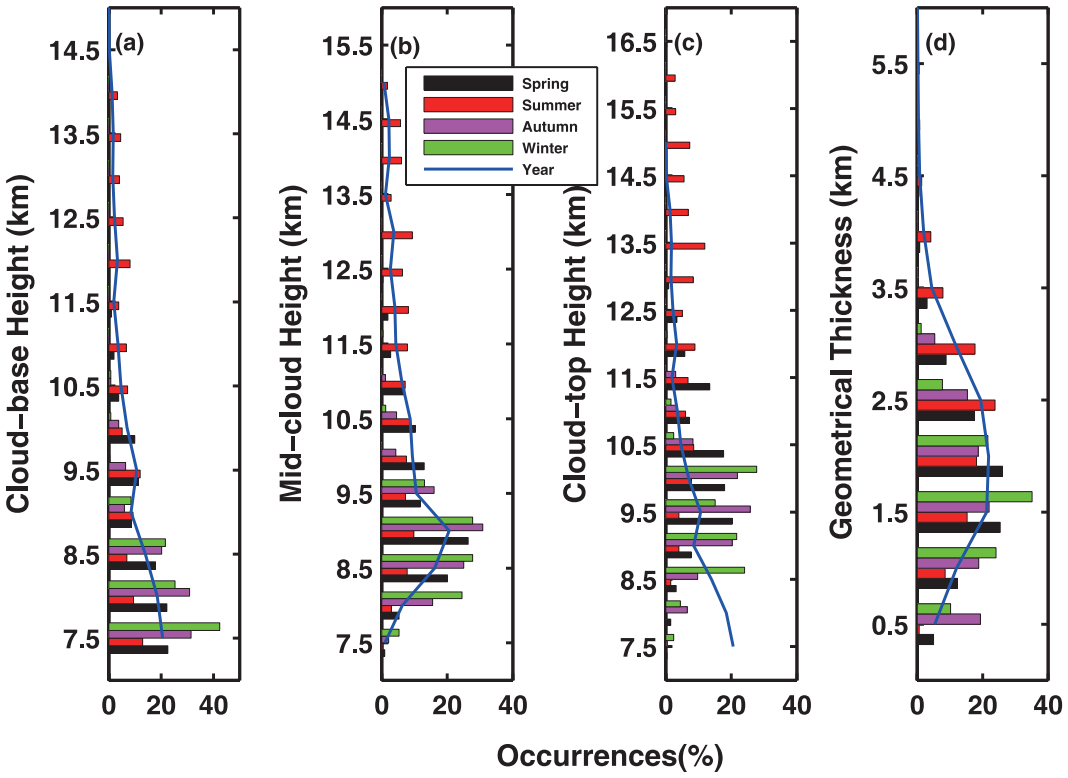


**Fig. 8.** Probability distributions of cirrus geometrical properties for each season (horizontal bars) and annual means (solid lines): (a) cloud-base height; (b) mid-cloud height; (c) cloud-top height; (d) geometrical thickness.

the cirrus extinction coefficient ($\sigma$), and $\tau_c$ over Taihu are investigated. In the case of sub-visible cirrus, the Fernald retrieval relation (Fernald, 1984) is insensitive to estimates of LR. For such cases encountered in this study, the cirrus LR is set to 24 sr. This value represents the mean of all retrieved cirrus LR for clouds with $\tau < 0.3$ found in the study. This approach has been used by Das et al. (2009). Mean LR in spring, summer, autumn, and winter was $27.6 \pm 20.1$, $23.5 \pm 15.1$, $24.1 \pm 15.3$, and $25.3 \pm 16.7$ sr, respectively, with an annual mean LR of $25.3 \pm 17.7$ sr (Table 3). Sassen et al. (1989) simulated the backscattering-to-extinction ratio (1/LR) for hexagonal ice crystals and found that for thin-plate, thick plate, and column ice crystals, 1/LR is equal to 0.026 $sr^{-1}$, 0.086 $sr^{-1}$, and 0.038 $sr^{-1}$, respectively. Figure 9a shows the frequency occurrence of 1/LR calculated from data collected over Taihu. About 70% of the values fall between 0.025 $sr^{-1}$ and 0.055 $sr^{-1}$, with a peak at 0.035 $sr^{-1}$, suggesting that most of the cirrus clouds observed in our study consisted of column ice crystals. Values of 1/LR close to 0.2 $sr^{-1}$ are likely due to specular reflection caused by falling or horizontally-oriented ice crystals, especially if observed through a vertically-pointing lidar (Ansmann et al., 1992; Das et al., 2009). Seasonal and annual mean LR as a function of mid-cloud height is shown in Fig. 9b. The LR is averaged over every 1 km height bin and vertical bars represent the standard deviation of the annual mean LR. There is no obvious correlation between LR and mid-cloud heights. This may be due to large variations in ice crystal mode and size and is also likely due to the process that forms cirrus clouds over the site.

In this study, $\sigma$ ranged from 0.001 to 1.59 $km^{-1}$, with an annual mean of $0.25 \pm 0.31$ $km^{-1}$ (Table 3). Seasonal mean $\sigma$ values were $0.23 \pm 0.35$ (spring), $0.19 \pm 0.19$ (summer), $0.37 \pm 0.56$ (autumn), and $0.20 \pm 0.40$ $km^{-1}$ (winter). Mean $\sigma$ as a function of mid-cloud height in each season and over the entire study period is shown in Fig. 10. The mean $\sigma$ is averaged over every 1 km height bin and the standard deviations of the annual mean $\sigma$ are shown as vertical bars. On the whole, the mean $\sigma$ decreased with increasing mid-cloud height in each season and year-round. Others have shown that $\sigma$ increases with mid-cloud temperature (Pace et al., 2003; Das et al., 2010), which is consistent with this study because higher mid-cloud heights are usually associated with relatively lower temperatures.

For all cirrus cloud cases in this study, $\tau_c$ ranged from 0.001 to 2.475, with mean values of $0.31 \pm 0.24$, $0.40 \pm 0.33$, $0.34 \pm 0.30$, and $0.20 \pm 0.20$ in spring, summer, autumn, and winter, respectively. The annual mean was $0.34 \pm 0.33$ (Table 3). Clouds with different $\tau_c$ play different roles when it comes to cloud radiative effects, which depend on cloud composition and geometrical thickness. Cirrus clouds here are classified into three cloud categories: sub-visible cloud ($\tau_c < 0.03$), optically thin cloud ($0.03 < \tau_c < 0.3$), and optically dense cloud ($\tau_c > 0.3$) (Seifert et al., 2007; Das et al., 2009). Table 3 lists the optical properties of cirrus cloud in each of these categories for all seasons and year-round. Num-

**Table 3.** Seasonal and annual mean optical properties of sub-visible, thin, and dense cirrus. Standard deviations are given in parentheses.

| | All | | | Sub-visible | | Thin | | | Dense | | |
|---|---|---|---|---|---|---|---|---|---|---|---|
| | $\sigma*$ (km$^{-1}$) | $\tau*$ | LR (sr)* | $\sigma$ (km$^{-1}$) | $\tau$ | $\sigma$ (km$^{-1}$) | $\tau$ | LR (sr) | $\sigma$ (km$^{-1}$) | $\tau$ | LR (sr) |
| Spring | 0.23 | 0.31 | 27.6 | 0.017 | 0.016 | 0.123 | 0.16 | 24.7 | 0.38 | 0.53 | 32.6 |
| | (0.35) | (0.24) | (20.1) | (0.022) | (0.009) | (0.100) | (0.08) | (19.7) | (0.47) | (0.19) | (19.2) |
| Summer | 0.19 | 0.40 | 23.5 | 0.011 | 0.015 | 0.094 | 0.16 | 19.4 | 0.29 | 0.65 | 28.1 |
| | (0.19) | (0.33) | (15.1) | (0.009) | (0.009) | (0.064) | (0.08) | (13.7) | (0.19) | (0.31) | (14.3) |
| Autumn | 0.37 | 0.34 | 24.1 | 0.024 | 0.015 | 0.160 | 0.15 | 21.6 | 0.70 | 0.63 | 27.2 |
| | (0.56) | (0.30) | (15.3) | (0.025) | (0.009) | (0.155) | (0.07) | (14.7) | (0.70) | (0.23) | (14.2) |
| Winter | 0.20 | 0.20 | 25.3 | 0.021 | 0.014 | 0.128 | 0.13 | 25.9 | 0.54 | 0.52 | 28.6 |
| | (0.40) | (0.20) | (16.7) | (0.015) | (0.009) | (0.167) | (0.07) | (15.7) | (0.70) | (0.20) | (16.6) |
| Year | 0.25 | 0.34 | 25.3 | 0.016 | 0.016 | 0.120 | 0.16 | 23.6 | 0.43 | 0.60 | 28.5 |
| | (0.31) | (0.30) | (17.7) | (0.020) | (0.009) | (0.107) | (0.08) | (17.2) | (0.43) | (0.35) | (16.8) |

*$\sigma$, extinction coefficient; $\tau$, optical depth; LR, lidar ratio.

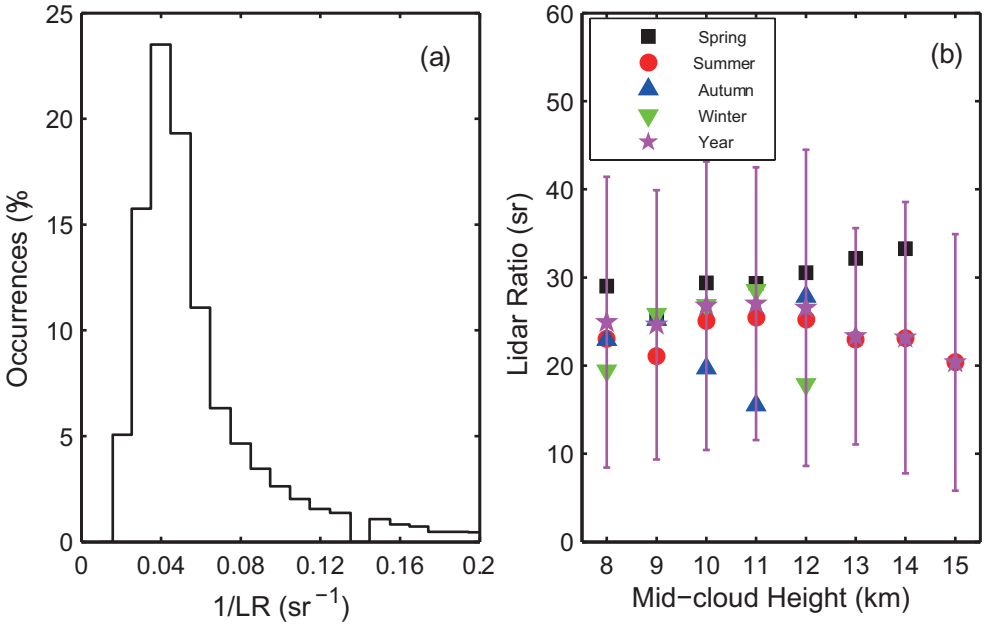


**Fig. 9.** (a) Frequency distribution of 1/LR over Taihu from June 2008 to May 2009 and (b) seasonal and annual mean LR as a function of mid-cloud height.

bers in parentheses are standard deviations. For all analyzed cirrus cloud cases, ~12% of the cases were sub-visible cirrus, ~43% were thin cirrus, and 45% were dense cirrus. Significant differences in the magnitude of $\sigma$ for all three categories of cirrus cloud are found.

### 4.3. *Comparisons with lidar-based retrievals*

For the sake of a proper comparison, we summarize information about midlatitude cirrus clouds detected by ground-based and space-borne lasers from studies made over the past decade (Table 4). A large range of cirrus CBH can occur. For example, at the Obsérvatoire de Haute Provence (OHP) and Site Instrumental de Recherche par Télédétection Atmosphérique (SIRTA) sites in France, they range from 7–13 km, and over the Clouds and the Earth's Radiant Energy System (CERES) Ocean Validation Experiment (COVE) and SGP sites in the U. S., cirrus CBH ranges from 7 km to 15 km

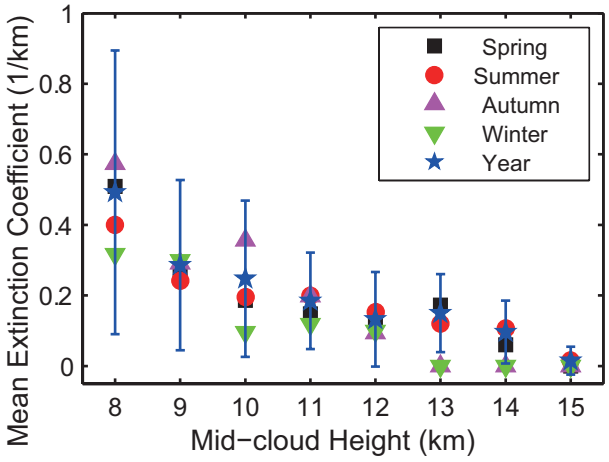


**Fig. 10.** Seasonal and annual mean extinction coefficient as a function of mid-cloud height.

**Table 4.** Summary of results from studies about midlatitude cirrus detected by ground-based and space-borne lasers made over the past decade.

| Location* | Time | Instruments | BH (km)** | TH (km)** | GT (km)** | LR (sr)** | $\tau$ | S/Thin/Dense*** (%) | Reference |
|---|---|---|---|---|---|---|---|---|---|
| OHP/France (44°N, 6°E) | 1997–99 | Lidar | n/a | n/a | $1.40 \pm 1.30$ | 18 (assumption) | n/a | 20 ($\tau < 0.03$) | Goldfarb et al. (2001) |
| Salt Lake City/U.S. (40.8°N, 111.8°E) | 1986–96 | Lidar | 8.8 | 11.2 | 1.81 | n/a | n/a | 16/35/48 | Sassen and Cambpell (2001) |
| Salt Lake City/U.S. (40.8°N, 111.8°E) | 1991–99 | Lidar | $8.2 \pm 2.0$ | $11.0 \pm 1.7$ | $2.79 \pm 1.38$ | $24 \pm 38$ | $0.75 \pm 0.91$ | 30 ($\tau < 0.3$) | Sassen and Comstock (2001) |
| Prestwick/Scotland (55.5°N, 4.6°W) | Sep–Oct 2000 | Lidar | 8.0 | 9.5 | 1.40 | 23 | 0.28 | $\sim 20$ ($\tau < 0.03$) | Immler and Schrems (2002) |
| Punta Arenas/Chile (53.1°S, 70.9°W) | Mar–Apr 2000 | Lidar | 8.3 | 9.6 | 1.20 | 26 | 0.27 | $\sim 20$ ($\tau < 0.03$) | Immler and Schrems (2002) |
| Thessaloniki/Greece (40.6°N, 22.9°E) | 2000–06 | Lidar | $9.0 \pm 1.1$ | $11.7 \pm 0.9$ | $2.70 \pm 0.90$ | $30 \pm 17$ | $0.31 \pm 0.24$ | 3/57/40 | Giannakaki et al. (2007) |
| Chuang-Li/China (24.6°N, 121.1°E) | 1999–2006 | Lidar | $12.3 \pm 2.2$ | $14.4 \pm 1.9$ | $2.08 \pm 1.20$ | $23 \pm 16$ | $0.16 \pm 0.27$ | 38/47/15 | Das et al. (2009) |
| Buenos Aires/Argentina (34.6°S, 58.5°W) | 2001–05 | Lidar | $9.6 \pm 0.9$ | $12.8 \pm 0.9$ | $2.41 \pm 0.95$ | n/a | n/a | n/a | Lakkis et al. (2009) |
| SGP/U.S. (37°N, 98°W) | Jul 2006 | Lidar | $9.6 \pm 1.8$ | $11.2 \pm 1.6$ | $1.57 \pm 0.99$ | n/a | n/a | 5/50/>40 | Dupont et al. (2010) |
| | Jun 2008 | (CALIOP) | $(9.9 \pm 2.1)$ | $(11.4 \pm 2.1)$ | $(1.57 \pm 0.93)$ | | | | |
| COVE/U.S. (37°N, 76°W) | Jul 2006 | Lidar | $9.8 \pm 1.8$ | $11.6 \pm 1.6$ | $1.85 \pm 0.97$ | n/a | n/a | 10/50/40 | Dupont et al. (2010) |
| | Jun 2008 | (CALIOP) | $(9.7 \pm 2.0)$ | $(11.2 \pm 2.1)$ | $(1.54 \pm 0.92)$ | | | | |
| OHP/France (44°N, 6°E) | Jul 2006 | Lidar | $9.2 \pm 1.5$ | $11.0 \pm 1.3$ | $1.85 \pm 1.03$ | n/a | n/a | 20/60/20 | Dupont et al. (2010) |
| | Jun 2008 | (CALIOP) | $(9.2 \pm 1.5)$ | $(11.0 \pm 1.5)$ | $(1.43 \pm 0.80)$ | | | | |
| SIRTA/France (47°N, 2°E) | Jul 2006 | Lidar | $9.7 \pm 1.7$ | $10.8 \pm 1.4$ | $1.17 \pm 0.95$ | n/a | n/a | 20/60/20 | Dupont et al. (2010) |
| | Jun 2008 | (CALIOP) | $(9.7 \pm 2.0)$ | $(10.5 \pm 1.6)$ | $(1.47 \pm 0.82)$ | | | | |
| North China (35°–45° N, 110°–120°E) | Jun 2006 | CALIOP | $9.2 \pm 1.8$ | $10.8 \pm 1.7$ | $1.60 \pm 1.15$ | n/a | $0.41 \pm 0.68$ | 30/35/35 | Min et al. (2010) |
| | May 2008 | | | | | | | | |
| Taihu/China (31.7°N, 120.4°E) | Jun 2008 | Lidar | $8.9 \pm 1.7$ | $10.7 \pm 1.9$ | $1.83 \pm 0.91$ | $25 \pm 17$ | $0.34 \pm 0.33$ | 12/43/45 | This study |
| | May 2009 | | | | | | | | |

*: OHP = Observatoire de Haute Provence; SGP = Southern Great Plains; COVE = Clouds and the Earth's Radiant Energy System (CERES) Ocean Validation Experiment; SIRTA = Site Instrumental de Recherche par Télédétection Atmosphérique

**: BH = base height; TH = top height; GT = geometrical thickness; LR = lidar ratio

***: S = sub-visible cloud; Thin = optically thin cloud; and Dense = optically dense cloud, based on Sassen and Cho (1992). n/a: no data available.

(Dupont et al., 2010). In this study, cirrus CBH ranges from 7 km to 14 km. Mean cirrus base heights range from 8 to 10 km in most of the studies listed in Table 4. One site (Chung-Li) has a relatively high base height of greater than 12 km (Das et al., 2009). The mean base height from the studies presented in Table 4 (excluding Chung-Li) is around 9.2 km, which is considered a typical base height for midlatitude cirrus clouds. The mean cloud-base height in this study ($8.9 \pm 1.7$ km) is comparable to this typical value. As listed in Table 4, mean cirrus cloud-top heights range from 9.5 km to 14.4 km, with most located around 11 km. The mean value (excluding Chung-Li) is about 11.0 km, which is close to the value found in this study ($10.7 \pm 1.9$ km). A study on the global characterization of cirrus using CALIPSO data (not shown in Table 4) has also shown that, between 20°N and 60°N, cirrus clouds with base and top altitudes at 8 km and 11 km, respectively, occur most often and that there are no significant differences in the vertical distribution of cirrus clouds between (20°–60°N) and (20°–60°S) (Nazaryan et al., 2008). Although cloud thickness generally has a broad distribution, e.g., from about 7.0 km over Salt Lake City (Sassen and Comstock, 2001) and Chung-Li (Das et al., 2009), and ranging from 0.5 km to 5 km over French and American sites (Dupont et al., 2010), most cirrus cloud thicknesses are less than 2.0 km. The mean cirrus thickness over Taihu was $1.83 \pm 0.91$ km, which is slightly larger than that found over the OHP (Goldfarb et al., 2001), Prestwick and Punta Arenas (Immler and Schrems, 2002), and SIRTA (Dupont et al., 2010) sites, and less than that over Salt Lake City (Sassen and Comstock, 2001), Thessaloniki (Giannakaki et al., 2007), and Buenos Aires (Lakkis et al., 2009). Averaging all values from Table 4, the typical thickness of midlatitude cirrus clouds is 1.7 km. Based on cirrus data sets derived using different detection techniques, Dowling and Radke (1990) reported that a typical global value for cirrus cloud thickness is 1.5 km.

The mean LR in this study was $25 \pm 17$ sr for all cirrus cloud cases, which falls within the range of values shown in Table 4. Using lidar data from Salt Lake City, Sassen and Comstock (2001) calculated a mean LR of about $24 \pm 38$ sr and a median value of ~27 sr. They also reported that the mean LR for anvil cirrus, and cirrus formed from synoptic flows and from orographic effects, is $\sim 24 \pm 43$ sr, $26 \pm 40$ sr, and $20 \pm 35$ sr, respectively. The mean LR for midlatitude cirrus in the Northern Hemisphere over Thessaloniki from 2000 to 2006 was $30 \pm 17$ sr (Giannakaki et al., 2007). From two studies made at Chung-Li (Chen et al., 2002; Das et al., 2009), values of $29 \pm 12$ sr and $23 \pm 16$ sr were found, respectively. A similar value of 23 sr was found over Prestwick during September to October 2000 (Immler and Schrems, 2002). At a site in the Southern Hemisphere, a mean value of 26 sr was calculated from data collected in March and April of 2000 (Immler and Schrems, 2002). Results found in this study are consistent with those from these earlier works. The LR depends on the properties of ice crystals and is also influenced by the height of the cirrus cloud. For example, in the study over Chung-Li, the LR varied randomly below 12 km and varied between 20 sr to 40 sr from 12–15 km, and 10 sr to 30 sr from 15–16 km (Chen et al., 2002).

The variability in $\tau_c$ depends on the composition and thickness of the cloud (Sivakumar et al., 2003). From the study by Sassen and Cho (1992), approximately 60% of cirrus clouds are optically thin and, over Chung-Li, more than 80% of the cirrus cases are optically thin (Das et al., 2009). Overall, most midlatitude cirrus clouds are optically thin and occur 60% of the time. The frequency of sub-visible cirrus in this study is approximately 12%, which is much higher than the 3% reported by Giannakaki et al. (2007) over Thessaloniki and the 5% reported by Dupont et al. (2010) over the SGP site. It is significantly lower than the 38% reported by Das et al. (2009) over Chung-Li. The frequency of subvisible cirrus in this study is roughly in line with that from studies of midlatitude cirrus over the COVE site (Dupont et al., 2010), at the OHP (Goldfarb et al., 2001; Dupont et al., 2010), Salt Lake City (Sassen and Campbell, 2001), Prestwick (Immler and Schrems, 2002), Punta Arenas (Immler and Schrems, 2002), the SIRTA (Dupont et al., 2010) sites, and northern China (Min et al., 2010). Since most midlatitude cirrus clouds are optically thin, the mean value of $\tau_c$ is generally less than 1.0. The mean $\tau$ for all cirrus clouds in this study is $0.34 \pm 0.33$, which is consistent with the mean values of 0.31 reported by Giannakaki et al. (2007) and 0.28 reported by Immler and Schrems (2002). However, the mean value found in this study is significantly larger than the value of $0.16 \pm 0.27$ reported by Das et al. (2009) and slightly smaller than the value of $0.41 \pm 0.68$ reported by Min et al. (2011). The mean value of $\tau_c$ is much smaller than that of $0.75 \pm 0.91$ reported by Sassen and Campbell (2001).

These differences are expected due to the variability in cirrus clouds arising from factors such as synoptic conditions, water vapor amount, and number of cloud condensation nuclei (Sassen and Campbell, 2001; Min et al., 2010). In addition, discrepancies may also arise from artifacts caused by instrument characteristics, such as lidar vertical resolution, maximum pulsed energy, receiver solid signals and so on, as well as from different methods used to retrieve optical properties and to correct for multiple scattering. Different ways of identifying/defining a cirrus cloud can also result in differences in their optical properties. For example, Das et al. (2009) define a cirrus cloud as the lowest cloud with a base height located above 8 km, while Wang and Sassen (2001, 2002) and Dupont et al. (2010) use a value of 7 km for the lowest cirrus CBH. An even smaller value of 5 km was used in the studies by Nazaryan et al. (2008) and Min et al. (2010) using CALIPSO data. Other observed variables such as $R_B(z)$ and lidar depolarization ratio can also be used to identify cirrus clouds. Discrepancies in any of these can contribute to differences in retrieved cirrus cloud properties.

## 5. Conclusion

Towards gaining insights into the characteristics of aerosols, clouds, and their interactions in southeastern China, a heavily polluted area in East Asia, a suite of instruments,

including a depolarization-sensitive MPL, was installed at Taihu, located in the center of the Yangtze Delta region, from May 2008 to December 2009. The seasonal patterns and the diurnal cycles of CF and CBH, and the vertical structure and optical properties of cirrus clouds, were first examined. Although only one year's worth of data were collected, they provide a useful first look at the characteristics of clouds, especially cirrus clouds, over this part of the world. The measurements collected also provide the opportunity to make comparisons with similar clouds in other regions of the world.

Overall, clouds were observed 41% of the time over the site throughout the campaign, and varied seasonally with a typical summer minimum (27.7%) and a winter maximum (51.4%). These results are similar to those reported in a study based on ground-based radar-lidar observations over the SGP site from 1997 to 2002. In most months, more clouds were found at night than during the day. On average, the largest/smallest seasonal CF occurred in winter/summer during the day, while the largest/smallest value at night occurred in spring/summer. Annual average CF experienced a significant diurnal cycle with amplitudes of about 24.6%. Cloud amounts decreased noticeably from the beginning of the day to midday, and then continuously increased from local noon to the end of the day. Annual mean CBHs were $3.05 \pm 2.73$, $2.46 \pm 2.08$, and $3.51 \pm 3.07$ km for all clouds, daytime clouds only, and nighttime clouds only, respectively. The highest CBHs were found in spring and summer, especially during the night. The largest number of detected cloud bases fell within the range of 0.5 km to 1.0 km. The annual mean diurnal cycle of CBH shows that low CBH occurred around noon and high CBHs appeared around midnight. The seasonal mean diurnal cycle of CBH was strong in spring and summer and relatively weak in autumn and winter.

Cirrus clouds comprised $\sim$36.2% of nighttime cloud observations with peaks in occurrence during the summer. Cirrus base heights ranged from 7 km to 14.3 km. More than 56% of cirrus base heights were located between 7 km and 8.5 km. Cirrus top heights showed a broad (7–16 km) and multi-modal distribution, with more than 40% of top heights appearing in the range of 9–10.5 km. Most of the cirrus cloud cases had thicknesses less than 3 km. Annual mean cirrus base and top heights were $8.89 \pm 1.65$ km and $10.73 \pm 1.86$ km, respectively. The annual mean thickness was $\sim 1.83 \pm 0.91$ km. The mean LR for all cirrus cloud cases in our study was $\sim 25 \pm 17$ sr, with a smooth seasonal variation. Approximately 70% of LRs fell within 18–40 sr, with a peak at 29 sr. No obvious relation between seasonal and annual mean LR and mid-cloud height was found. Large ranges in the magnitudes of cirrus $\sigma$ (0.001–1.59 km$^{-1}$) and cirrus $\tau$ (0.001–2.475) were observed. Annual mean cirrus cloud $\sigma$ and $\tau$ were $0.25 \pm 0.31$ km$^{-1}$ and $0.34 \pm 0.33$, respectively. Approximately 12% of the cirrus cloud cases were sub-visible cirrus, 43% were thin cirrus, and 45% were dense cirrus. Thicker cirrus clouds occurred more frequently during the summer than in winter. Cirrus geometrical and optical properties derived in this study are similar to those reported in other studies using lasers to detect midlatitude cirrus clouds.

***Acknowledgements.*** This study was supported by the Ministry of Science and Technology of China (Grant Nos. Change: 2013CB955802 to 2012AA120901), State Laboratory of Earth Surface Process and Resource Ecology, National Science Foundation of China (41175019), and the US Department of Energy (Grant Nos. DEFG0208ER64571and DE-SC0007171). The authors are grateful to Prof. Zhien WANG, University of Wyoming, for providing the cloud mask code.

## REFERENCES

Ansmann, A., U. Wandinger, M. Riebesell, C. Weitkamp, and W. Michaels, 1992: Independent measurement of extinction and backscatter profiles in cirrus clouds by using a combined Raman elastic backscatter lidar. *Appl. Opt.*, **31**, 7113–7131.

Bissonnette, L. R., G. Roy, and G. Tremblay, 2007: Lidar-based characterization of the geometry and structure of water clouds. *J. Atmos. Oceanic Technol.*, **24**(8), 1364–1376.

Campbell, J. R., and M. Shiobara, 2008: Glaciation of a mixed-phase boundary layer cloud at a coastal arctic site as depicted in continuous lidar measurements. *Polar Science*, **2**(2), 121–127.

Campbell, J. R., D. L. Hlavka, E. J. Welton, C. J. Flynn, D. D. Turner, J. D. Spinhirne, V. S. Scott, and I. H. Hwang, 2002: Full-time, eye-safe cloud and aerosol lidar observation at Atmospheric Radiation Measurement Program sites: Instrument and data processing. *J. Atmos. Oceanic Technol.*, **19**, 431–442.

Chang, F. L., and Z. Li, 2005: A new method for detection of cirrus overlapping water clouds and determination of their optical properties. *J. Atmos. Sci.*, **62**, 3993–4009.

Chen, W. N., C. W. Chiang, and J. B. Nee, 2002: Lidar ratio and depolarization ratio for cirrus clouds. *Appl. Opt.*, **41**, 6470–6476.

Clothiaux, E. E., G. G. Mace, T. P. Ackerman, T. J. Kane, J. D. Spinhirne, and V. S. Scott, 1998: An automated algorithm for detection of hydrometeor returns in micro pulse lidar data, *J. Atmos. Oceanic Tech.*, **15**, 1035–1042.

Comstock, J. M., and K. Sassen, 2001: Retrieval of cirrus cloud cadiative and backscattering properties using combined Lidar and Infrared Radiometer (LIRAD) measurements. *J. Atmos. Oceanic Technol.*, **18**(10), 1658–1673.

Comstock, J. M., T. P. Ackerman, and G. G. Mace, 2002: Ground-based lidar and radar remote sensing of tropical cirrus clouds at Nauru Island: Cloud statistics and radiative impacts. *J. Geophys. Res.*, **107**(D23), AAC 16-1–AAC 16-14, doi: 10.1029/2002JD002203.

Das, S. K., C. W. Chiang, and J. B. Nee, 2009: Characteristics of cirrus clouds and its radiative properties based on lidar observation over Chung-Li, Taiwan. *Atmos. Res.*, **93**(4), 723–735.

Das, K, S., J. B. Nee, and C. W. Chiang, 2010: A LiDAR study of the effective size of cirrus ice crystals over Chung-Li, Taiwan. *J. Atmos. Sol.-Terr. Phys.*, **72**(9–10), 781–788.

Dessler, A. E., and P. Yang, 2003: The distribution of tropical thin cirrus clouds inferred from terra MODIS data. *J. Climate*, **16**, 1241–1247.

Dong, X. Q., P. Minnis, and B. K. Xi, 2005: A climatology of mid-latitude continental clouds from ARM SGP site: Part I. Low-level cloud macrophysical, microphysical and radiative properties. *J. Climate*, **18**, 1391–1410.

Dong, X. Q., B. K. Xi, and P. Minnis, 2006: A climatology of

mid-latitude continental clouds from the ARM SGP Central Facility: Part II: Cloud fraction and surface radiative forcing. *J. Climate*, **19**, 1765–1783.

Dong, X. Q., B. K. Xi, K. Crosby, C. N. Long, R. S. Stone, and M. D. Shupe, 2010: A 10 year climatology of Arctic cloud fraction and radiative forcing at Barrow, Alaska. *J. Geophys. Res*., **115**, D17212, doi: 10.1029/2009JD013489.

Dowling, D. R., and L. F. Radke, 1990: A summary of the physical properties of cirrus clouds. *J. Appl. Meteor*., **29**(9), 970–978.

Dupont, J. C., M. Haeffelin, Y. Morile, V. Noel, P. Keckhut, D. Winker, J. Comstock, and A. Roblin, 2010: Macrophysical and optical properties of mid-latitude cirrus clouds from four ground-based lidars and collocated CALIOP observations. *J. Geophys. Res*., **115**, D00H24, doi: 10.1029/2009JD011943.

Dupont, J. C., M. Haeffelin, Y. Morille, J. M. Comstock, C. Flynn, C. N. Long, C. Sivaraman, and R. K. Newson, 2011: Cloud properties derived from two lidars over the ARM SGP site. *Geophys. Res. Lett*., **38**, L08814, doi: 10.1029/2010GL046274.

Fernald, F. G., 1984: Analysis of atmospheric lidar observations: Some comments. *Appl. Opt.*, **23**, 652–653.

Flynn, C. J., A. Mendoza, Y. Zheng, and S. Mathur, 2007: Novel polarization-sensitive micropulse lidar measurement technique. *Optics Express*, **15**(6), 2785–2790.

Giannakaki, E., D. S. Balis, V. Amiridis, and S. Kazadzis, 2007: Optical and geometrical characteristics of cirrus clouds over a Southern European lidar station. *Atmos. Chem. Phys.*, **7**, 5519–5530.

Goldfarb, L., P. Keckhut, M. L. Chanin, and A. Hauchecorne, 2001: Cirrus climatological results from lidar measurements at OHP (44°N, 6°E). *Geophys. Res. Lett.*, **28**(9), 1687–1690.

Immler, F., and O. Schrems, 2002: LIDAR measurements of cirrus clouds in the northern and southern mid-latitudes during INCA (55 °N, 53 °S): A comparative study. *Geophys. Res. Lett.*, **16**, 56-1–56-4, doi: 10.1029/2002GL015077.

IPCC, 2007: *Climate Change 2007: The Physical Science Basis. Contribution of Working Group I to the Forth Assessment Report of the Intergovernmental Panel on Climate Change*, S. Solomon et al., Eds. Cambridge University Press, Cambridge, United Kingdom and New York, NY, USA, 996 pp.

Keckhut, P., A. Hauchecorne, S. Bekki, A. Colette, C. David, and J. Jumelet, 2005: Indications of thin cirrus clouds in the stratosphere at mid-latitudes. *Atmos. Chem. Phys*., **5**(12), 3407–3414.

Kollias, P., G. Tselioudis, and B. A. Albrecht, 2007: Cloud climatology at the Southern Great Plains and the layer structure, drizzle, and atmospheric modes of continental stratus. *J. Geophys. Res.*, **112**(D9), D09116, doi: 10.1029/2006jd007307.

Lakkis, S. G., M. Lavorato, and P. O. Canziani, 2009: Monitoring cirrus clouds with lidar in the Southern Hemisphere: A local study over Buenos Aires. 1. Tropopause heights. *Atmos. Res.*, **92**, 18–26.

Li, Z., and Coauthors, 2007: Preface to special section on East Asian Studies of Tropospheric Aerosols: An International Regional Experiment (EAST-AIRE). *J. Geophys. Res.*, **112**(D22), doi: 10.1029/2007JD008853.

Li, Z., and Coauthors, 2011: East Asian Studies of Tropospheric Aerosols and their Impact on Regional Climate (EAS-TAIRC): An overview. *J. Geophys. Res*., **116**, D00K34, doi: 10.1029/2010JD015257.

Liu, J., Y. Zheng, Z. Li, C. Flynn, E. J. Welton, and M. Cribb, 2011: Transport, vertical structure and radiative properties of dust events in southeast China determined from ground and space sensors. *Atmos. Environ.*, **45**(35), 6469–6480.

Mace, G. G., Q. Zhang, M. Vaughan, R. Marchand, G. Stephens, C. Trepte, and D. Winker, 2009: A description of hydrometeor layer occurrence statistics derived from the first year of merged CloudSat and CALIPSO data. *J. Geophys. Res.*, **114**, D00A26, doi: 10.1029/2007JD009755.

Mahesh, A., J. R. Campbell, and J. D. Spinhirne, 2005: Multiyear measurements of cloud base heights at South Pole by lidar. *Geophys. Res. Lett*., **32**, L09812, doi: 10.1029/2004GL021983.

Min, M., P. C. Wang, J. R. Campbell, X. M. Zong, and Y. Li, 2010: Midlatitude cirrus cloud radiative forcing over China. *J. Geophys. Res*., **115**(D20), doi: 10.1029/2010JD014161.

Min, M., P. Wang, J. R. Campbell, X. Zong, and J. Xia, 2011: Cirrus cloud macrophysical and optical properties over north China from CALIOP measurements. *Adv. Atmos. Sci.*, **28**(3), 653–664, doi: 10.1007/s00376-010-0049-5.

Nazaryan, H., M. P. McCormick, and W. P. Menzel, 2008: Global characterization of cirrus clouds using CALIPSO data. *J. Geophys. Res.*, **113**, D16211, doi: 10.1029/2007JD009481.

Noel, V., D. M. Winker, T. J. Garrett, and M. Mcgill, 2007: Extinction coefficients retrieved in deep tropical ice clouds from lidar observations using CALIPSO like algorithm compared to in-situ measurements from cloud integrating nephelometer during CRYSTAL-FACE. *Atmos. Chem. Phys.*, **7**, 1415–1422.

Pace, G., M. Cacciani, A. di Sarra, G. Fiocco, and D. Fuà, 2003: Lidar observations of equatorial cirrus clouds at Mahé Seychelles. *J. Geophys. Res*., **108**(D8), 4236, doi: 10.1029/2002JD002710.

Platnick, S., M. D. King, S. A. Ackerman, W. P. Menzel, B. A. Baum, J. C. Riedi, and R. A. Frey, 2003: The MODIS cloud products: Algorithms and examples from Terra. *IEEE T. Geosci. Remote*, **41**(2), 459–473.

Reichardt, J., 1999: Optical and geometrical properties of northern midlatitude cirrus clouds observed with a UV Raman lidar. *Phys. Chem. Earth, Part B*, **24**, 255–260.

Sassen, K., and B. S. Cho, 1992: Subvisual-thin cirrus lidar dataset for satellite verification and climatological research. *J. Appl. Meteor*., **31**, 1275–1285.

Sassen, K., and J. R. Campbell, 2001: A midlatitude cirrus cloud climatology from the facility for atmospheric remote sensing. Part I: Macrophysical and synoptic properties. *J. Atmos. Sci.*, **58**, 481–496.

Sassen, K., and J. M. Comstock, 2001: A mid-latitude cirrus cloud climatology from the facility for atmospheric remote sensing. Part III: Radiative properties. *J. Atmos. Sci.*, **58**, 2113–2127.

Sassen, K., M. K. Griffin, and G. C. Dodd, 1989: Optical scattering and microphysical properties of subvisual cirrus cloud, and climatic implications. *J. Appl. Meteor*., **28**, 91–98.

Sassen, K., Z. E. Wang, and D. Liu, 2008: Global distribution of cirrus clouds from Cloud-Sat/Cloud-Aerosol Lidar and Infrared Pathfinder Satellite Observations (CALIPSO) measurements. *J. Geophys. Res.*, **113**, doi: 10.1029/2008JD009972.

Seifert, P., A. Ansmann, D. Müller, U. Wandinger, D. Althausen, A. J. Heymsfield, S. T. Massie, and C. Schmitt, 2007: Cirrus optical properties observed with lidar, radiosonde, and satellite over the tropical Indian Ocean during the aerosol-polluted northeast and clean maritime southwest monsoon. *J. Geophys. Res.*, **112**, doi: 10.1029/2006JD008352.

Shupe, M. D., V. P. Walden, E. Eloranta, T. Uttal, J. R. Campbell,

S. M. Starkweather and M. Shiobara, 2011: Clouds at arctic atmospheric observatories. Part I: Occurrence and .acrophysical properties. *J. Appl. Meteor. Climatol*., **50**, 626–644.

Sivakumar, V., Y. Bhavanikumar, P. B. Rao, K. Mizutani, T. Aoki, M. Yasui, and T. Itabe, 2003: Lidar observed characteristics of the tropical cirrus clouds. *Radio Sci*., **38**(6), doi: 10.1029/2002RS002719.

Spinhirne, J. D., J. A. R. Rall, and V. S. Scott, 1995: Compact eye safe lidar systems. *Rev. Laser Eng.*, **23**, 112–118.

Stephens, G. L., 2005: Cloud feedbacks in the climate system: A critical review. *J. Climate*, **18**, 237–273.

Stubenrauch, C. J., A. Chedin, G. Radel, N. A. Scott, and S. Serrar, 2006: Cloud properties and their seasonal and diurnal variability from TOVS Path-B. *J. Climate*, **19**, 5531–5553.

Sunilkumar, S. V., K. Parameswaran, and B. V. Thampi, 2008: Interdependence of tropical cirrus properties and their variability. *Ann. Geophys*., **26**(3), 413–429.

Thorsen, T. J., Q. Fu, J. M. Comstock, C. Sivaraman, M. A. Vaughan, D. M. Winker, and D. D. Turner, 2013: Macrophysical properties of tropical cirrus clouds from the CALIPSO satellite and from ground-based micropulse and Raman lidars. *J. Geophys. Res.*, **118**, 9209–9220.

Vukicevic, T., O. Coddington, and P. Pilewskie, 2010: Characterizing the retrieval of cloud properties from optical remote sensing. *J. Geophys. Res.*, **115**, D20211, doi: 10.1029/2009JD012830.

Wang, Z., and K. Sassen, 2001: Cloud type and macrophysical property retrieval using multiple remote sensors. *J. Appl. Meteor*., **40**(10), 1665–1682.

Wang, Z., and K. Sassen, 2002: Cirrus cloud microphysical property retrieval using lidar and radar measurements. Part II: Mid-latitude cirrus microphysical and radiative properties. *J. Atmos. Sci*., **59**(14), 2291–2302.

Wang, Z. Z., R. L. Chi, B. Liu, and J. Zhou, 2008: Depolarization properties of cirrus clouds from polarization lidar measurements over Hefei in spring. *Chinese Optics Letters*, **6**(4), 235–237.

Winker, D. M., J. R. Pelon, and M. P. McCormick, 2003: The CALIPSO mission: Spaceborne lidar for observation of aerosols and clouds. *Proc. SPIE*, **4893**, doi: 10.1117/12.466539.

Wu, Y. H., S. K. Chaw, B. Gross, F. Moshary, and S. Ahmed, 2009: Low and optically thin cloud measurements using a Raman-Mie lidar. *Appl. Opt.*, **48**(6), 1218–1227.

Zhang, M. H., and Coauthors, 2005: Comparing clouds and their seasonal variations in 10 atmospheric general circulation models with satellite measurements. *J. Geophys. Res*., **110**, D15S02, doi: 10.1029/2004JD005021.

Zhao, C. F., Y. Z. Wang, Q. Q. Wang, Z. Q. Li, Z. E. Wang, and D. Liu, 2014: A new cloud and aerosol layer detection method based on micropulse lidar measurements. *J. Geophys. Res.*, **119**, 6788–6802, doi: 10.1002/2014JD021760.